



PAPER • OPEN ACCESS

Particle image based simultaneous velocity and particle concentration measurement

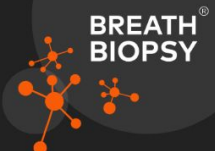
To cite this article: Abhilash Sankaran *et al* 2024 *Meas. Sci. Technol.* **35** 065206

View the [article online](#) for updates and enhancements.

You may also like

- [Statistics of the Voronoï cell perimeter in large bi-pointed maps](#)
Emmanuel Guitter
- [Quantification of the atomic surfaces and volumes of a metal cluster based on the molecular surface model](#)
Yifan Yu and Junzhi Cui
- [Statistical topology of perturbed two-dimensional lattices](#)
Hannes Leipold, Emanuel A Lazar, Kenneth A Brakke et al.

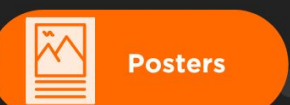
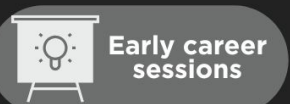
Breath Biopsy Conference



Join the conference to explore the **latest challenges** and advances in **breath research**, you could even **present your latest work!**



5th & 6th November
Online



Register now for free!

Particle image based simultaneous velocity and particle concentration measurement

Abhilash Sankaran* , Rainer Hain and Christian J Kähler

University of the Bundeswehr Munich, Institute of Fluid Mechanics and Aerodynamics,
Werner-Heisenberg-Weg 39, Neubiberg 85577, Germany

E-mail: abhilash.sankaran@unibw.de

Received 27 November 2023, revised 29 February 2024

Accepted for publication 14 March 2024

Published 21 March 2024



CrossMark

Abstract

The aim of this study is the expansion of the application of particle image velocimetry (PIV) to include the determination of particle concentration within the visualized area, in addition to velocity analysis. The assessment of particle concentration is valuable in various lab-scale experiments involving particle dispersion. Additionally, it plays a crucial role in evaluating the quality of PIV images. The research investigates two particle image-based concentration techniques: the exponential averaging-based sliding method and the Voronoi cell-based method on the particle images. The exponential averaging method provides a straightforward approach, utilizing a constant length scale for sliding average application to particle images. However, this method may result in broadened interfaces or a ‘marker-shot’ effect at low concentrations, making it less suitable for scenarios involving highly non-uniform particle distributions, such as concentrated jet emissions into ambient environments. Consequently, detecting interfaces in such cases requires additional effort for reliable results. In contrast, the Voronoi cell-based technique offers the advantage of spatially adaptive resolution, making it well-suited for variable concentration distributions and situations where interface detection is crucial. To comprehensively evaluate the performance of these techniques, a synthetic test case was generated to simulate a diffusion problem featuring an initial step in concentration distribution. Both the exponential averaging and Voronoi cell-based methods were applied and compared using this synthetic test case. Additionally, the effect of particle–particle overlap is analyzed theoretically and experimentally with uniform concentration and comparison with particle counter measurements. A modified Voronoi method is introduced, providing flexibility in capturing a wide range of concentration regions and features. An example experimental scenario involving a turbulent puff was considered demonstrating the application of the developed methods. The results demonstrate that the Voronoi method effectively captures small structures with high concentrations while providing reliable results in regions with low concentrations.

Supplementary material for this article is available [online](#)

Keywords: particle concentration, particle image velocimetry, diffusion, Voronoi cells, exponential moving average

* Author to whom any correspondence should be addressed.



1. Introduction

In many fluid mechanical systems, the concentrations of the species are time and/or space dependent. Dispersed phase analysis is important in the context of solid/liquid particles in liquid/gaseous flows for analyzing the flow fields as well as heat and mass exchange rates in a variety of systems (Nishino *et al* 2000). Concentration field measurements are useful to understand the spatial distribution of the particle concentration in various scenarios including detection of boundaries of the species or mixing effectiveness, to name a few (Gnirß and Tropea 2008). Typical methods involve a point measurement sensor system like particle counter. Point measurement techniques, however, encounter difficulties when there is need for instantaneous spatial information on physical properties such as velocity and concentration. Additionally, most point measurement systems like particle counters sample part of the air to count the particles. Therefore, it is intrusive to the system being measured and can only provide an average in longer duration of the test.

For many scenarios involving aerosol dispersion analysis like air pollution (Saïd *et al* 2005, Zhang *et al* 2020, Newland and Woods 2023), bio-aerosol transmission studies (Shah *et al* 2021, Kähler *et al* 2023), indoor air quality (Tang *et al* 2020, Kähler *et al* 2023), a thorough understanding of flow features, direction, and fluctuations in species concentration is imperative to assess air quality. Mean point-wise properties would not be sufficient; instead, comprehending the spatial and temporal variations in concentration becomes essential. Moreover, it is crucial to determine if the sampled air is representative of the sensed region (Vincent 2007). Achieving this requires a quantitative understanding of aerosol dispersion characteristics in flows, enabling a better grasp of the chances of successful aerosol sampling. Remote sensing of aerosols also necessitates this knowledge to optimize detection capabilities. By gaining insight into the dispersion behavior of aerosols, one can effectively maximize their ability to sample aerosols and gather valuable data for further analysis and decision-making.

Particle image velocimetry (PIV) and particle tracking velocimetry (PTV) are instantaneous whole-field fluid velocity measurement techniques based on imaging of particle tracers. These methods make it possible to detect spatial flow structures and provide information of the spatial differential quantities of turbulence. In this work, the goal is to determine particle concentration within the field of view in addition to the velocity information. This leverages data from pre-existing flow tracers, as opposed to employing tracer gases. Furthermore, in addition to concentration measurements as detailed, the particle concentration within the visualization window is also important for assessing the quality of the PIV images and the resultant velocity field.

An image-based method proposed previously is based on intensity of the scattered laser light from particles (Gnirß and Tropea 2008). However, the method involves many corrections to obtain physical concentrations of which uneven illumination and stray reflections pose difficulty to correct reliably. Another approach utilizing image intensity information

is the autocorrelation of the image acquired (Nguyen *et al* 2012, Warner and Smith 2014). The peak of the autocorrelation is related to the intensity within the interrogation window and can be utilized to derive particle concentration within the window. While these methods are simple to apply, they still depend on reliable background subtraction and appropriate interrogation window selection.

In the present work, methods based on individual particle images are discussed. One of the methods is the exponential sliding average method for concentration determination. It needs to be emphasized that the length scale is fixed once chosen and cannot be varied within the image even if the concentration of the particle images is drastically different. Another method introduced here is based on Voronoi cells, which in principle is an adaptive grid procedure to calculate the local particle concentration. Such method has been demonstrated for application in the cosmological application (Schaap and Van De Weygaert 2000). However, for fluid mechanical measurements only few such considerations are available. Monchaux *et al* (2010) analyzed clustering of particles in turbulent flows utilizing Voronoi cells. Weber *et al* (2023) applied Voronoi cells for evaluation of bubbly flows. One method for interface determination in multiphase flows is presented by Li *et al* (2021) where a complementary to Voronoi cells—the Delaunay meshing technique—is applied. Some methods discussed above (Schaap and Van De Weygaert 2000, Li *et al* 2021) focus in getting the sharp features present in the respective applications: cosmological and multiphase flows. However, when one is interested in a particle concentration field encompassing vastly different scales, it is not straightforward to apply the above methods. This consideration, which has not been explored previously, holds significance for practical inquiries related to particle cloud dispersion or emitted particle plumes. In this work, methods based on PIV particle images for particle concentration determination for fluid mechanical applications are presented and analyzed in detail. Particular focus has been applied to Voronoi cell method, which could be applied for variety of real scenarios involving drastically different concentrations like pollution studies, indoor air quality to name a few.

2. Particle concentration measurement

This study primarily focuses on the particle image based concentration measurement based on two techniques: (a) sliding average method; (b) Voronoi cell based method.

2.1. Sliding average method

The sliding average method is a technique that averages the dataset by considering a moving window of data points. Here, an exponential moving average type filter, which applies a local filter to compute the average particle per pixel as below is utilized (Lukin 2007),

$$\Upsilon^{\text{avg}}(i) = \left(1 - \frac{1}{l}\right) \Upsilon^{\text{avg}}(i-1) + \left(\frac{1}{l}\right) \Upsilon(i) \quad (1)$$

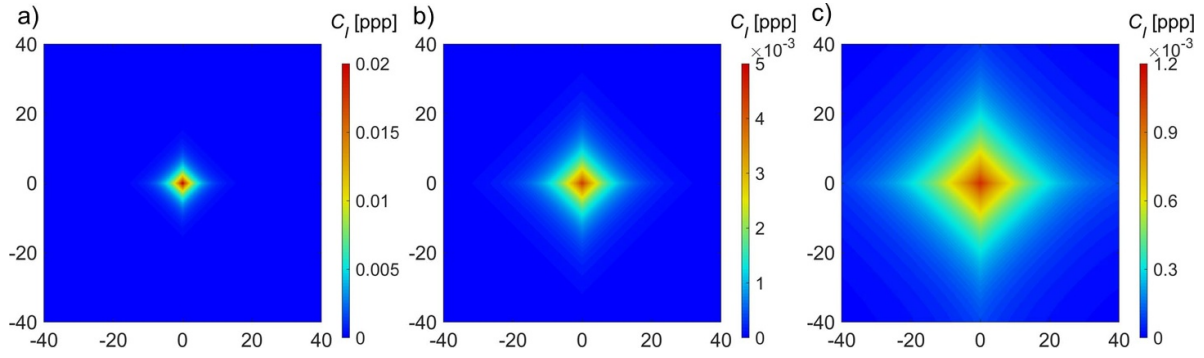


Figure 1. The contour of the variation of the local C_l value with one particle at $(0, 0)$ for different length scales for the sliding average: (a) $l = 4$ pixels; (b) $l = 8$ pixels; (c) $l = 16$ pixels. The axis dimensions are in pixels.

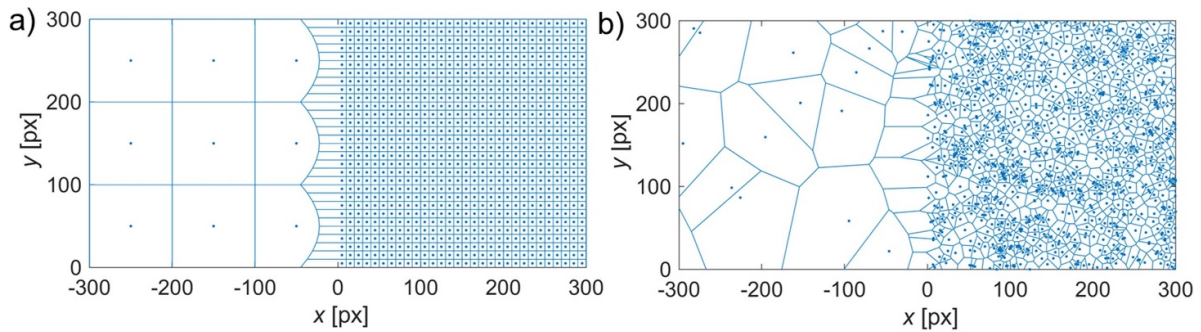


Figure 2. (a) The Voronoi cells around uniformly spaced particles with concentrations $C_1 = 10^{-4}$ ppp and $C_2 = 0.01$ ppp to the left and right of origin, respectively. (b) Voronoi cells around practically uniform distribution with Brownian diffusion with the same concentrations $C_1 = 10^{-4}$ ppp and $C_2 = 0.01$ ppp to the left and right of origin, respectively.

$\Upsilon(i)$ is the intensity at a certain pixel i and Υ^{avg} is the computed intensity value at pixel i and $i - 1$, accordingly. l is the length scale in pixel chosen for the average computation. The same method is applied in all four directions one after the other to compute the sliding average value of the intensity values (Lukin 2007). For simplicity, the technique is referred to as sliding average method from this point forward.

Figure 1 illustrates the results obtained from the sliding average method with a single particle located at position $(0, 0)$. Prior to applying the sliding average, the value at this location is 1, indicating one particle at the center pixel (1 particle per pixel, 1 ppp). It is assumed here that the particle images are available as binary representations (ones and zeros) to focus on the technique. Further details on how these binary images might be obtained from PIV images are detailed later in the experimental section. The method effectively redistributes the particle into all four directions after passes in all directions as given by equation (1). For example at length scale $l = 4$ px, the peak value is $C_l \sim 0.02$ ppp at the center and progressively decreases to 0 as the distance from the defined length scale increases. Notably, the peak value diminishes with an increase in the averaging length scale, while the influence of the particle extends further as the length scale grows. This still maintains the sum of the values in the domain to be 1.

Figure 1 reveals the importance of choosing an appropriate length scale for the calculation of the sliding average method. On the one hand, there must be enough particles within the

chosen length scale to reveal the average particles in the window. On the other hand, the difference in the value must signify the change in concentration rather than the effect of a single particle.

2.2. Voronoi cell based method

The Voronoi cell surrounding a point (or particle) defines a polygonal region encompassing the points closest to it and forming a closed network with neighboring cells without any overlaps or gaps (Okabe *et al* 2000, Schaap and Van De Weygaert 2000). An illustrative example of Voronoi cells with uniformly spaced particles with different spacing (concentration) in either side of origin is shown in figure 2(a). Figure 2(b) depicts the Voronoi cells for the case with macroscopically same concentration; however, the particles are randomly distributed as expected in practical case with Brownian motion.

The inverse of the cell area technically represents the number of particles per unit area, which can be interpreted as particle density or concentration. This can be visualized as true for the perfect case as shown in figure 2(a) which is similar to calculation of the unit cell as done in material science (Callister and Rethwisch 2018). However, in the context of fluid mechanics, the distribution of particles is less ordered as shown in figure 2(b) with Brownian diffusion. Hence, the above measure has to be rewritten to necessarily

reflect concentration in the traditional continuum sense and not focus on individual particles.

To address this, one can approximate the continuum by either considering a sufficiently large number of particles or selecting an appropriate examination window size. Here, we consider K number of nearest neighbor cells to calculate the average area of the K cells and the inverse of this average area is the local concentration centered at the particle considered.

In addition, one is also interested in approximating the local concentration when there are few particles in the domain. This is particularly important when one needs to distinguish the low concentration and high concentration regions either in time or space and not averaging the entire set for sufficiently high number of particles.

An alternate approach to Voronoi method is to utilize the Delaunay triangles for the calculation of the concentration. However, it was found that the size distribution of the Delaunay triangles for practically uniform cases varied significantly, resulting in a broad distribution compared to the Voronoi cell sizes. This results in the need of a larger number of triangles for convergence to macroscopic concentration. The distribution obtained is presented in supplementary information. In this work, only the Voronoi method is explored further.

3. Results and discussion with synthetic generated images

3.1. Test case

For comparison of the different methods, a synthetic case of a diffusion problem is considered. A domain extending from $-10\,000\text{ px} < x < +10\,000\text{ px}$ and $0 < y < 1000\text{ px}$ is considered. An example multiplication factor considered here is $L = 1\text{ mm} = 10\text{ px}$ representative of realistic scenarios. The domain is closed by walls in x -direction. At $x = 0$, there is a removable wall, which is removed at $t = 0\text{ s}$. A periodic boundary condition is considered along the y -axis. Before removing the wall, uniformly placed particles with $C_1 = 10^{-4}\text{ ppp}$ and $C_2 = 0.01\text{ ppp}$ are considered at left ($x < 0$) and right ($x > 0$) of origin, respectively (figure 2(a)). Such concentrations are representative concentrations of cases when one can neglect particle–particle overlap, the effect of which is discussed later. Considering a concentration scale $C_0 = C_2 = 0.01\text{ ppp}$, the initial concentrations can be rewritten as $C_1/C_0 = 0.01$ and $C_2/C_0 = 1$. The diffusion process is modeled with applying diffusion jumps to each particle in the domain.

The diffusion jump Δr of a particle in a time step Δt is given by (Daune 1999, Sankaran *et al* 2020):

$$\Delta r = 2\sqrt{D\Delta t \log\left(\frac{1}{R}\right)} \quad (2)$$

where R is a random number between 0 and 1 defining the probability of the diffusion jump of length Δr . This jump Δr occurs in random direction θ with $0 \leq \theta \leq 2\pi$. A diffusion coefficient of $D = 10^{-5}\text{ m}^2\text{ s}^{-1}$ is assumed here and a time

step of 1 s is considered (where the physical scale $1\text{ mm} = 10\text{ px}$ is considered as before).

The diffusion process is run for extended time before time $t = 0\text{ s}$ resulting in a practically uniform concentration on both sides of the origin, as depicted in figure 2(b). At $t = 0\text{ s}$, the wall separating the two concentration side is removed.

For time scales $t \ll L_{0-w}^2/D$ (where $L_{0-w} = 1000\text{ mm} = 10\,000\text{ px}$ is the distance from center to the side walls), the concentration distribution for $t > 0$ (i.e. after the wall separating region is removed), can be compared to the analytical one-dimensional solution with an initial step in concentration. The analytical solution for the diffusion equation starting at $t = 0\text{ s}$ is given by (Balluffi *et al* 2005)

$$C = (C_2 - C_1) \left(\frac{1}{2} + \frac{1}{2} \operatorname{erf} \left(\frac{x}{\sqrt{4Dt}} \right) \right) + C_1. \quad (3)$$

One can test the capturing of the initial step in concentration with the methods detailed above. This gives the information on the characteristics of the interface determination by the method employed. The practical initial step distribution before the interaction between the two different concentration obtained at $t = 0\text{ s}$ is shown in figure 2(b) (which also depicts the Voronoi cells constructed around the points). Importantly, a reflective boundary condition is applied for all the sides and the corners for Voronoi cell construction, resulting in eight repetitions of the window of interest. This ensures that the cells within the region of interest have appropriate sizes, as the end points lead to open Voronoi cells.

The results for the instance $t = 0\text{ s}$ for the distribution shown in figure 2(b) following the sliding average method and Voronoi method are presented in figures 3 and 4, respectively. In the case of the sliding average method with length scale $l = 20\text{ px}$, one can observe that the higher concentration is captured in detail with the local fluctuations and also identifies the step change in concentration. However, at low concentration, one can see a marker-shot like noise with values falling near zero and peaking intermittently. This phenomenon arises from the insufficient presence of particles within the imposed length scale. Therefore, although the selected length scale is effective in capturing the step change and high concentrations, it is not that suitable at low concentrations. At larger length scale of sliding average of $l = 80\text{ px}$, the noise at lower concentration is present but considerably reduced. Further, the jump is broadened towards both the higher and lower concentrations.

In case of the Voronoi method, the effect of different numbers of nearest neighbors (K) averaged is shown in figure 4. With lower number of cells averaged, i.e. $K = 30$, concentration profile reveals all the features at small scales leading to the fluctuations at high concentrations. It is important to highlight that the marker-shot noise effect is eliminated with accounting for only $K = 30$ cells (cf figure 4(b)). Further, the jump in concentration is also captured reliably. When the number of averaged cells is increased, there is marginal improvement at low concentrations and some smoothing at high concentration (cf figure 4). However, the jump in concentration is notably diffused to larger length scales. It is interesting that the smoothing effect on the jump is more pronounced at lower

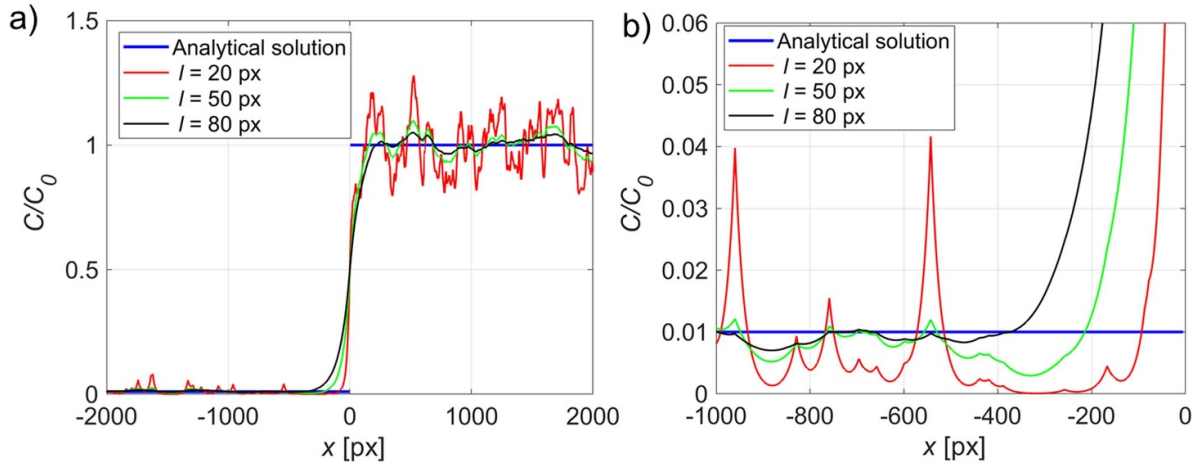


Figure 3. (a) Particle density distribution at $t = 0$ along the line $y = 500$ px obtained by the sliding average method, comparing the effect of the length scale l , and the analytical solution. (b) The zoomed-in view at the lower concentration region.

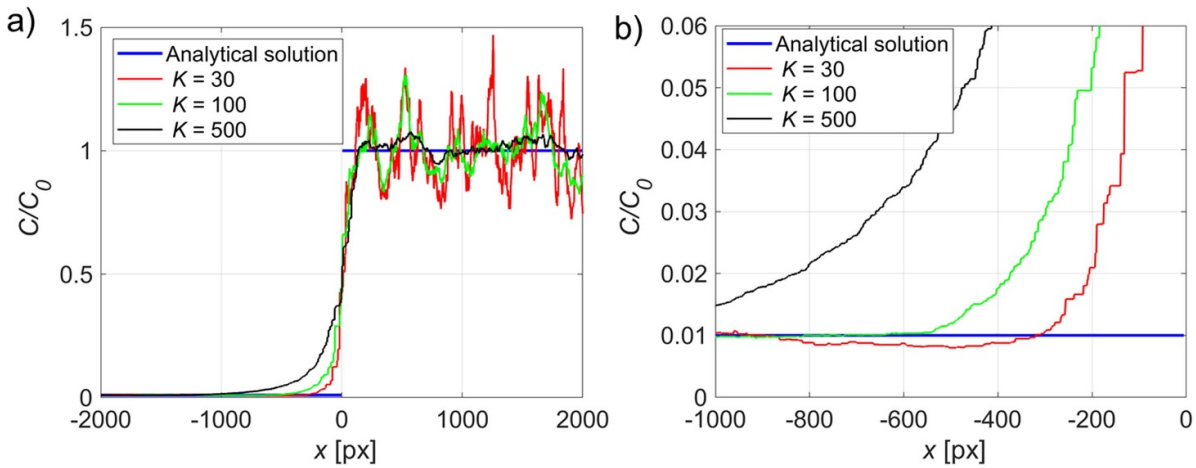


Figure 4. (a) Particle density distribution at $t = 0$ along the line $y = 500$ px obtained by the Voronoi method, comparing the effect of K and the analytical solution. (b) The zoomed-in view at the lower concentration region.

concentrations. In contrast, at higher concentrations, the jump remains relatively unsmoothed because the data from 100 or 500 points still falls within a relatively small physical scale.

3.2. Choosing the number of nearest neighbors K

A possible solution which can be easily implemented for the Voronoi method is to incorporate a criterion to choose the number of cells to be averaged depending on the local fluctuations.

Fluctuations due to Brownian motion: To choose a natural number of cells to average, one needs to understand the natural variation present within the uniform concentration regime. In this regard, let us consider the case of the practically uniform concentration in a closed space with Brownian diffusion. A large domain ($x \times y = 30\,000 \text{ px} \times 30\,000 \text{ px}$) with the overall non-dimensional concentration (C/C_0) of 1 is considered ($C_0 = 0.01 \text{ ppp}$). Specifically, 9×10^6 randomly distributed particles are considered within this domain.

Firstly, the Voronoi method is applied to the entire field to cover the entire space of interest. 1000 random points away

from the sides are chosen and the effect of averaging K number of nearest cells is observed. The resulting average concentration and spread of the data with the 1000 points chosen is shown in figures 5(a) and (b).

The interesting part is that this distribution can be combined together to a single distribution by applying the central limit theorem (Billingsley 1995). The obtained distribution is shown in figure 5(c). The obtained histogram follows the expected Gaussian profile as observed in figure 5(c). This is useful to understand the expected deviation in the concentration with K cells considered within the uniform concentration regions.

Consequently, this insight can be extended to non-uniformly distributed points, enabling us to anticipate the uncertainty associated with averaging K cells. This knowledge becomes a crucial factor in determining the appropriate value for K . Specifically, if the deviation within K cells surpasses a predefined threshold, reflecting a certain level of stringency, there may be limited benefit in further increasing the number of averaged cells. In fact, doing so might inadvertently obscure underlying features or concentration gradients by averaging the cells covering the entire variation. Therefore, opting for a

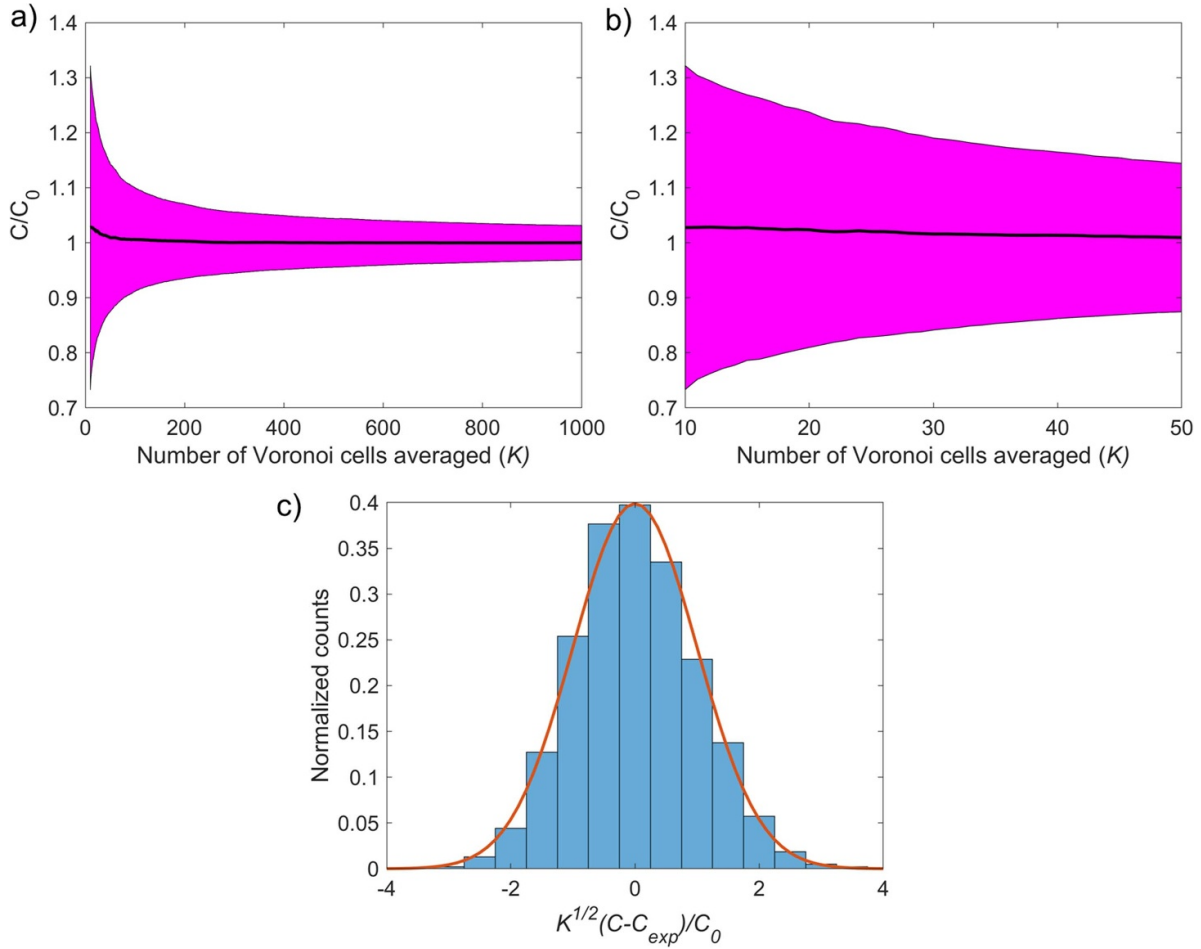


Figure 5. The concentration average and the standard deviation distribution with number of Voronoi cells averaged (K) from 10 to 1000. (b) Zoomed in view for $K = 10$ to $K = 50$. (c) The collapsed histogram of the normalized counts with scaling $K^{1/2}(C - C_{exp})/C_0$ with the overlaid Gaussian profile. The C_{exp} ($=1$) is the expected concentration.

smaller value of K could be more pertinent, as it has the potential to unveil these intricate details more effectively.

Cut-off criterion: By referring to the information given in figure 5, one can observe the expected deviation with averaging K number of cells. Here, we consider moving-mean of chosen K_C number of cells. For instance, if we take $K_C = 30$, the deviation (δ) is ~ 0.2 with respect to the expected value (cf figure 5(b)).

For the real case, however, the expected value is not known a priori and one needs to rely on the local mean. The available estimate for C_0 is the locally computed C_{Kc} . The variation of C_{Kc} itself has to be accounted for, which has highest probability to be within 0.8–1.2 times the expected value (cf figure 5(b)). The computed value C_{Kc} has highest probability to be within 0.8–1.2 times the expected value (cf figure 5(b)). Hence, the total relative deviation, relative to the mean at first K_C , expected could be considered as a criticality $\delta_{crit} \sim 0.5$ (2 times the deviation with respect to the expected, divided by the lower of the local value).

Following this reasoning, prior to averaging the nearest neighbor cells, one can monitor the variation of the moving mean. If the moving mean lies above/below the set δ_{crit} of the first K_C cell average, then there is significant change in the

concentration when farther cells are averaged. As a result, one can truncate the cells to be averaged. In other words, if the condition

$$\left| \frac{C_{mm}(i) - C_{Kc}}{C_{Kc}} \right| > \delta_{crit} \quad (4)$$

is fulfilled, then truncate the averaging at $K = i$ number of nearest neighbors corresponding to the point considered.

Here, $C_{mm}(i)$ represents the moving mean computed over K_C number of cells where i runs from the nearest to farthest cells from the cell in consideration. When K_C is odd, the window is centered around the element in the current cell. When K_C is even, the window is centered around the current and previous cells.

The above consideration is effectively truncating the number of averaged cells depending on the deviation when K is increased. The criticality can be generalized by following the scaling shown in figure 5(c) for any K_C :

$$\delta_{crit} = \frac{2.74}{K_C^{1/2}}. \quad (5)$$

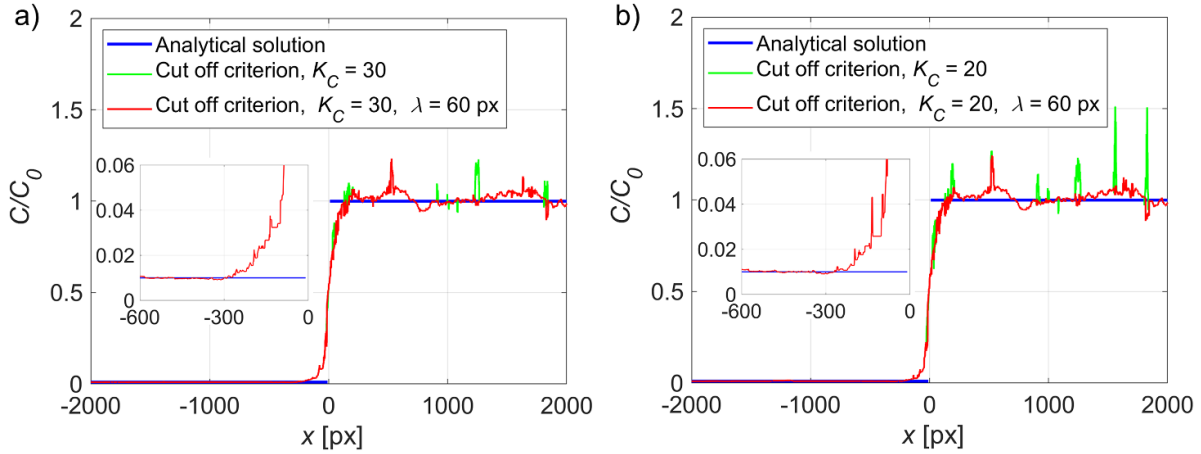


Figure 6. Particle density distribution at $t = 0$ s along the line $y = 500$ px obtained by the Voronoi method, comparing the effect of the cut-off criterion and minimum length scale $\lambda = 60$ px for (a) $K_C = 30$ and (b) $K_C = 20$. The blue line is the analytical solution and the inset shows the zoomed-in view at the transition to the lower concentration region.

The value 2.74 is the product $30^{1/2} \times 0.5$ as chosen above and the denominator generalizes for any K_C from the central limit theorem as expected from the figure 5(c).

The results for the synthetic diffusion case obtained by applying the cut off criterion (equation (4)) with $K_C = 30$ and $K_C = 20$ is shown in figures 6(a) and (b) respectively. In addition, if the length scale of truncated K cells is smaller than the minimum length scale (λ) chosen (selected spatial resolution) then continue with averaging following the same strategy before while ignoring the condition for truncation. This essentially acts like a filter for the fluctuations at very small scales as seen in figure 6. The minimum length does not change the results at the low concentration (cf insets in figure 6) as expected due to the farther spacing of the particles. These results indicate that the cut-off criterion effectively captures the jump in the concentration within small physical scale.

To compare the different methods at different time instances of the diffusion process, two time instances $t = 100$ s and $t = 500$ s are shown in figure 7. It can be seen that the concentration profiles obtained by both methods follow similar trend and fluctuate around the analytical solution. The sliding average method with $l = 80$ px is smoothed in comparison with the Voronoi method with cut-off criterion.

3.3. Theoretical consideration of particle image overlap

In the synthetic test case examined previously, it is supposed that all the particles in the visualized volume are detectable in the projected image as visualized by the cameras. However, in real-world scenarios, especially with an increase in concentration, particle image overlaps will occur. This means that as the physical concentration increases, the number of particle images will not reflect the actual number of the particles in the visualized image. The theoretical consideration of this effect is undertaken here.

Consider the total image area of A with N_p number of particles in the visualized thin volume. Assume a critical circular disc of area A_{crit} around the particle image in which

another particle image center falls for overlap to occur in the image. The total probable number of overlapping particle images, N_o , obtained from Poisson distribution of particles can be expressed as (Maas 1992, Cierpka *et al* 2013):

$$N_o = (N_p - 1) + \frac{A}{A_{\text{crit}}} \left(e^{-\frac{(N_p-1)A_{\text{crit}}}{A}} - 1 \right). \quad (6)$$

To obtain the effective information/detectable particle images visible with overlap, one needs to account for the probability of exactly m number of particles at the area considered A_{crit} (Maas 1992):

$$P(m) = \frac{\left(\frac{N_p A_{\text{crit}}}{A} \right)^m}{m!} e^{-\frac{N_p A_{\text{crit}}}{A}}. \quad (7)$$

The relative overlap probability (P_o) with j number of overlaps (i.e. $j = 1$ means there is exactly one other particle within the same A_{crit}) is calculated by

$$P_o(j) = \frac{P(j+1)}{1 - (P(0) + P(1))} \quad (8)$$

where $P(0)$ and $P(1)$ represent the probabilities of having no particle and just one particle within the area, respectively, both of which do not result in overlap. $P_o(j)$ indicates the probability of j overlaps occurring. The effective count of particles, or the number of detectable particle images within the image, is obtained by

$$N_d = N_p - \sum_{j=1}^{\xi} \frac{j}{j+1} P_o(j) N_o \quad (9)$$

where ξ is the total number of overlaps to be taken into account for all practically possible overlaps that occur. Here $\xi = 30$ is considered (where the probability of overlap is practically negligible with $P_o < 10^{-5}$).

One can define the density/concentration in the image plane when all the particles in the visualized volume are considered

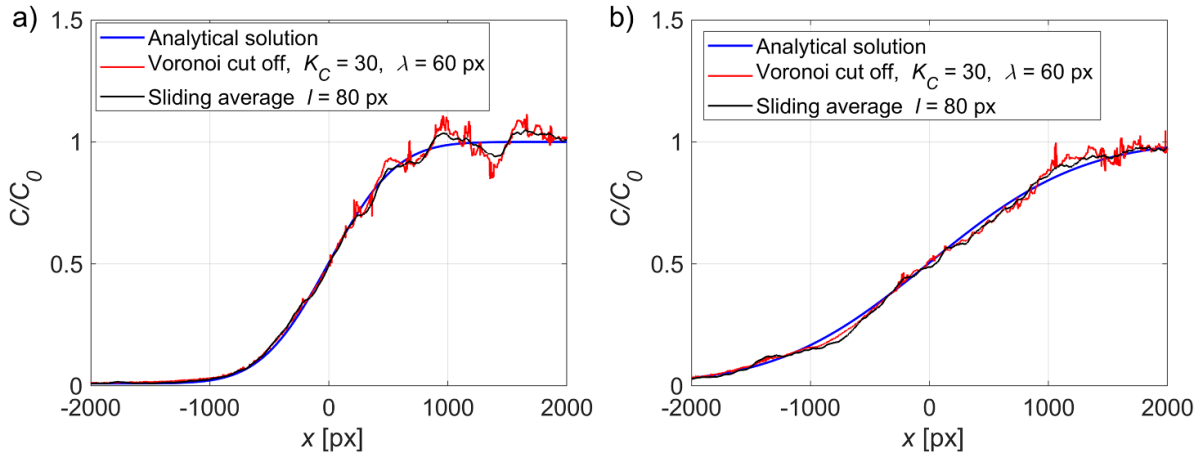


Figure 7. Particle density distribution obtained at time instances: (a) $t = 100$ s and (b) $t = 500$ s. The comparison is obtained along the line $y = 500$ px obtained by the Voronoi method, with cut-off criterion ($K_C = 30$) and minimum length scale $\lambda = 6$ mm and the sliding average method with $l = 80$ px. The blue line is the analytical solution (equation (3)).

as $\phi_a = N_p/A$, and the detectable number density of particle images is given by $\phi_d = N_d/A$. At very low concentrations, when the particle images are far from each other, the overlap probability is practically zero and one can expect $\phi_d \approx \phi_a$.

Now, the actual density of the particles in reality (C_a) in units of particles/cm³ is the density of the particles in the measurement volume. If one plots the graph of C_a vs. ϕ_d relationship from experimental data, the initial slope serves as the multiplication factor for ϕ_a , yielding theoretical concentration in physical space at very low physical concentrations. Further, at higher concentrations, depending on the value of A_{crit} the detected density of particle images ϕ_d deviates from the initial slope depending on the overlaps (equation (9)). The resulting theoretical curves and comparisons with experimental results are presented in the next section.

4. Experiments

4.1. Calibration

In real experiments, one can visualize the particles within the laser-illuminated sheet of certain thickness as done in PIV/PTV experiments. The physical concentration information from the visualized windows requires either the determination of the exact volume of the visualized window or calibration with a particle counter at constant concentration. Here, we take the approach with calibration with particle counter at uniform concentration in the room. More details are given in this section.

The measurement equipment is a stereoscopic PIV system consisting of two cameras, a laser, and a computer. The cameras are set at forward scattering mode w.r.t. the laser sheet (Prasad 2000). This results in substantial signal to noise ratio for accurate particle image detection. Two frames are taken which allows the calculation of the three velocity components in the measurement plane with stereoscopic PIV. Here, for concentration determination only information from one of the camera and one frame is utilized. However, in principle the

data from the other frame and other camera could also be considered in order to increase the accuracy of the concentration measurement.

For concentration calibration, the closed room was nebulized with DEHS particles (mean diameter ≈ 0.4 μm) and simultaneous measurements using a particle counter AQ Guard (Palas GmbH, Germany) were performed as reference. The obtained raw PIV images at different particle concentration are shown in figure 8(a). It is essential to underscore the importance of sharp particle images for accurate particle counting and is a critical consideration during experimental setup. The average particle image diameter varied between 1.5 and 2 px for the visualized images.

To count the particle images within the PIV snapshots, it is assumed that the particle images have 2D Gaussian intensity profiles. The local maxima (intensity peaks) are counted as a particle. Before applying this, a sliding local minimum is subtracted to remove background noise and an intensity threshold for the particle cutoff is selected. DaVis (LaVision 2021) is used for performing these steps. This method does lead to undercounting at high particle concentrations due to particle–particle overlap as explained earlier. However, the subsequent calibration, elaborated in this section, addresses this concern, provided that the image particle counts do not reach saturation.

The calibration of the particle image data to the physical concentration is needed to account for the spatial variation of the laser intensity, the non-constant light sheet thickness and shape, and the varying magnification factor. The distribution of the detected particle image concentration (ϕ_d) within the visualized image is shown in figure 8(b). Further, the resultant calibration curve at certain location in space obtained with Voronoi method is shown in figure 8(c). This revealed non-linearity in dependence of the observed particles per pixel to the physical concentration. A smoothing spline fit is obtained for all points in the x – y -plane as a function of concentration as shown in figure 8(c).

It can be observed that the particle image density ϕ_d increases linearly with physical concentration of particles at

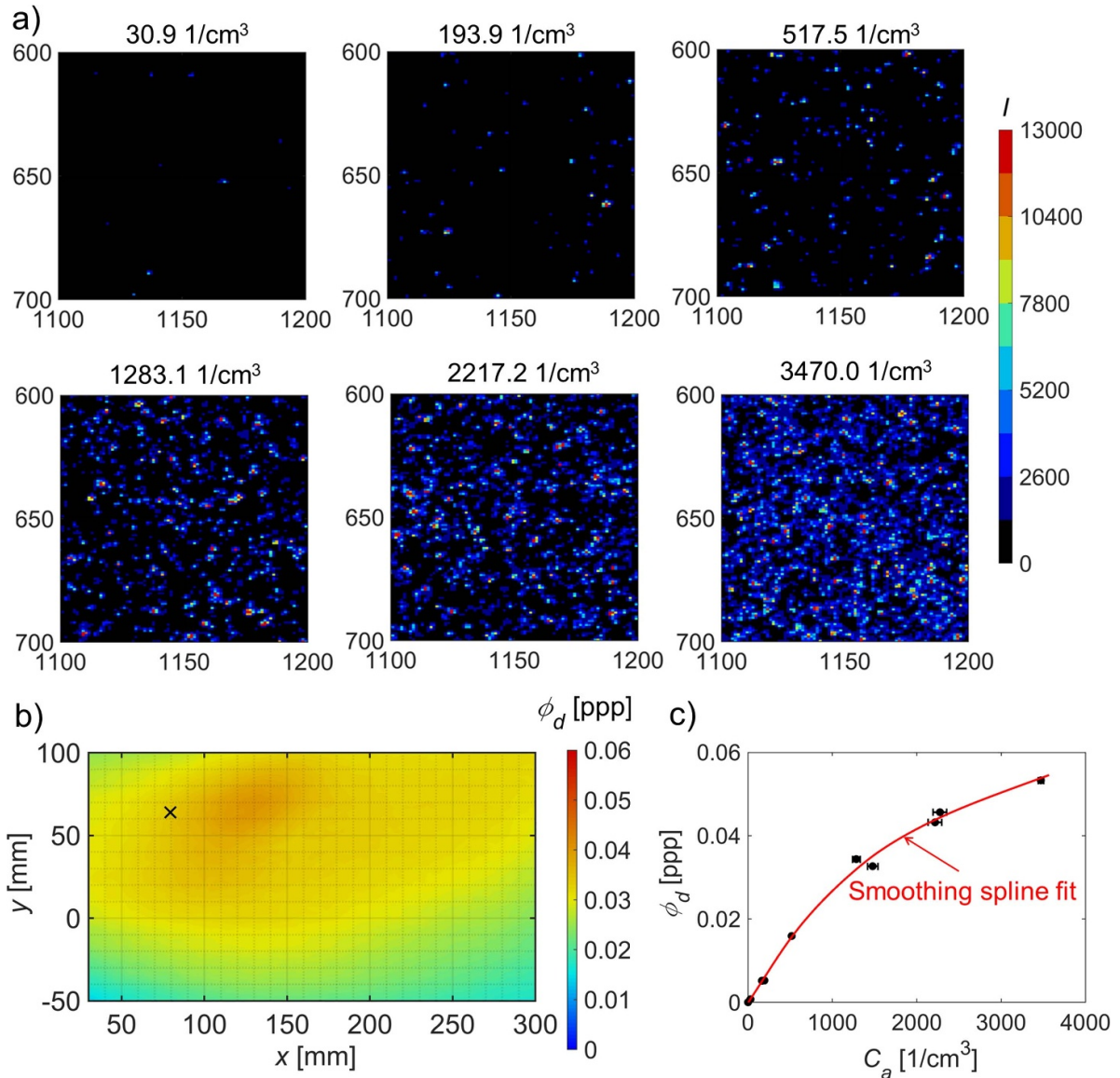


Figure 8. (a) The raw particle images at different physical concentrations, where I is the intensity in counts. The axis dimensions are in pixels. (b) Contour of the measured variation of ϕ_d (ppp) at a constant physical particle concentration of $C_a = 1283.1 \text{ cm}^{-3}$. The Voronoi method with intensity threshold of 800 counts is applied. (c) The experimental points of ϕ_d (ppp) at different physical particle concentrations C_a and the calibration function obtained at point location marked by \times in (b) as a smoothing spline fit. The error bars indicate the standard deviation of the particle counter measurements.

low concentrations and deviates around 500 cm^{-3} . However, with further increase in physical concentration, the particle image based density increase is more gradual. This indicates the effect of the particle image overlaps in the observed images. Consequently, the data obtained from visualization is directly proportional to the results from the particle counter, but only at low concentrations when particle overlap is negligible. As the physical concentration increases, the likelihood of particle overlap also rises. Next, we delve into a comparison of these results with theoretical description of the overlap effect described before.

The results obtained from the particle counter and that measured from the visualized window processed with different

intensity threshold are depicted in figure 9. For comparison, the results obtained from the theory presented in section 3.3 are overlaid. The theoretical curves generated are at different A_{crit} corresponding to 2.0–3.2 px (overlapping) disc diameter. The disc diameter is chosen in order to encompass the experimental results observed. It needs to be noted that the particle diameter in the images varied between 1.5 and 2 px for the visualized images. It is reasonable to assume that the overlapping disc diameter is of the order of the diameter of the particle images. The theoretical curves closely follow the experimental curve indicating the effect of the particle overlap. The theoretical curve corresponding to 3.2 px disc diameter aligns more closely with the experimental curve at a

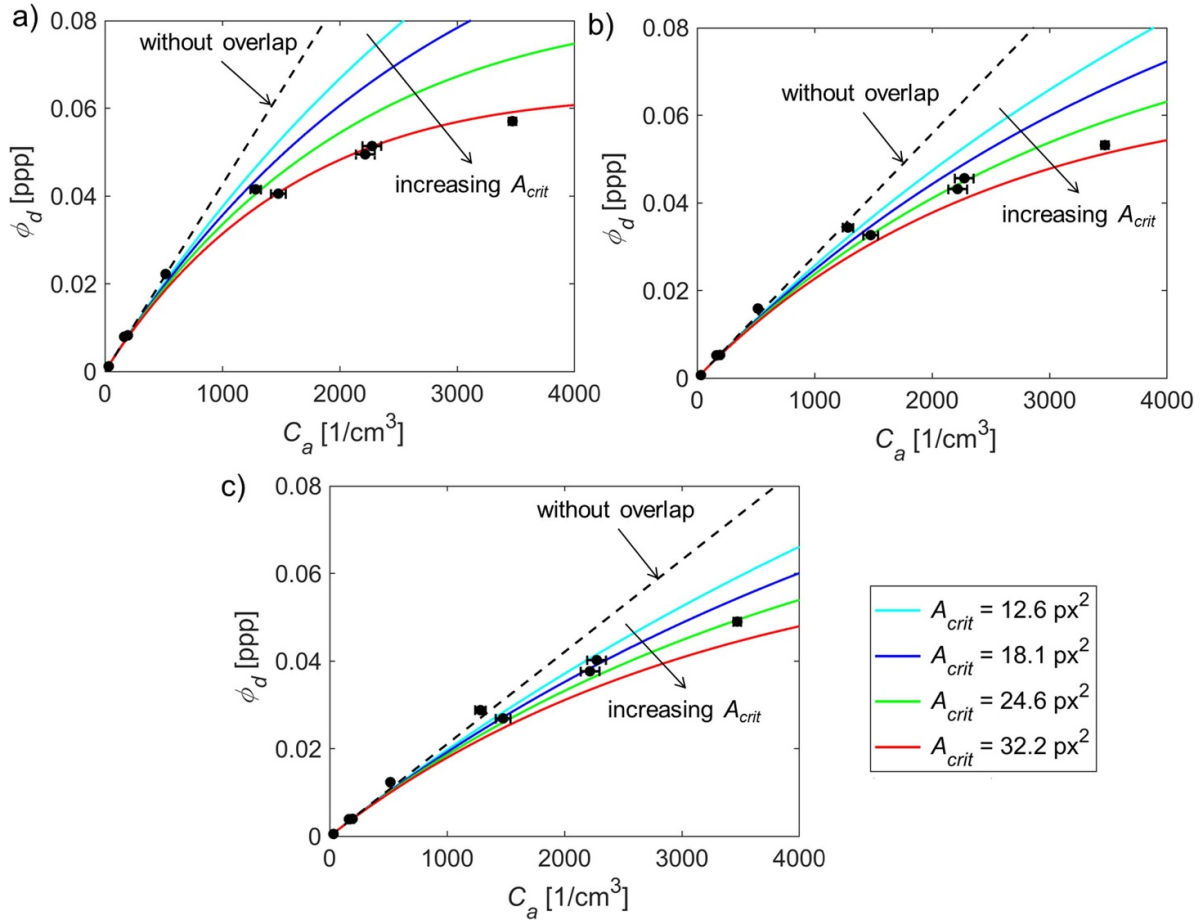


Figure 9. Comparison of the experimentally measured particle number density C_a from particle counter versus detected in the image (ϕ_d) and the theoretical values at different intensity threshold: (a) experimental intensity threshold of 400 counts; (b) experimental intensity threshold of 800 counts; (c) experimental intensity threshold of 1200 counts. The theoretical critical area (A_{crit}) corresponds to diameter of 2.0 (cyan), 2.4 (blue), 2.8 (green) and 3.2 (red) px. Further, the dashed line depicts the initial slope of the experimental data points which represents the theoretical curve if there were no overlaps.

lower intensity threshold of 400 (cf figure 9(a)). Conversely, the curve corresponding to 2.4/2.8 px disc diameter aligns more closely with the experimental curve at a higher intensity threshold of 1200 (cf figure 9(c)). The typical intensity of the particle image is expected to follow a Gaussian profile, so reducing the intensity threshold would lead to a larger effective particle image diameter, aligning with the observed trend. Further, the initial slope which represents the curve without overlap effect decreases as the intensity threshold increases. This indicates that the total particles considered decreases as the intensity threshold increases. Consequently, this reduction leads to reduced difference between the overlap curves and the curve without overlap at higher concentrations. At lower intensity thresholds (cf figure 9(a)), particle overlap results in a near saturation effect at higher concentrations. Hence, the overlap effect could be reduced by choosing higher intensity threshold.

It is important to note that the overlap effect is similar, regardless of whether one considers the sliding average method or the Voronoi method.

4.2. Measurement uncertainty analysis

The uncertainty of the measurements was assessed by applying the calibration function to one instance of each uniform concentration case. The calculated uncertainty ranges between 11% and 15% of particle counter measurements, considering maximum averaging of 100 cells for the Voronoi method. This variation aligns with the predicted $\sim 10\%$ expected variation within the uniform case with Brownian diffusion (figure 5). The additional uncertainty is due to the fitting function which also includes the particle–particle overlap effect. For the sliding average method, the calibration function was determined similarly with length scale $l = 16$ pixel. The uncertainty for this method is approximately $\sim 11\%$ at a concentration of 1283.1 cm^{-3} . While the uncertainty decreases slightly at higher concentrations, it significantly increases as the concentration decreases, attributed to marker-shot-like noise, as previously explained. Further, it needs to be emphasized that this approximation is for uniform concentration, and the uncertainty would increase with local gradients.

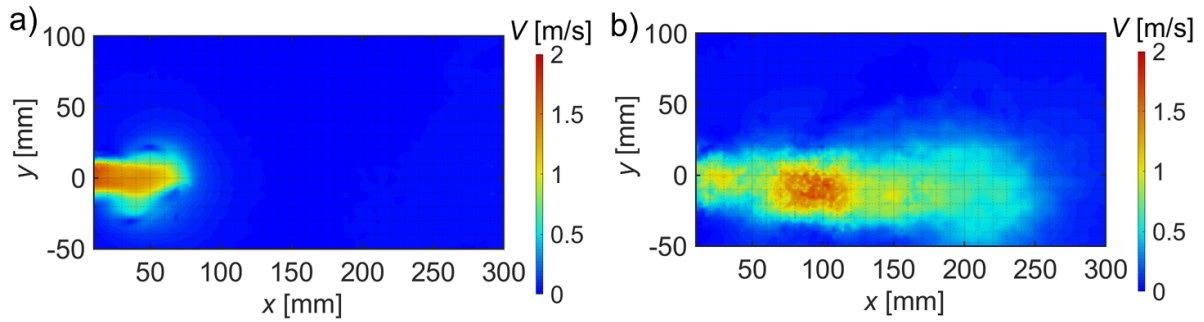


Figure 10. Average velocity magnitude (averaged with 10 cycles) contour at time instances: (a) t' (non-dimensionalized by the cycle time), and (b) $t' + 0.133$. Cycle time = 3.75 s.

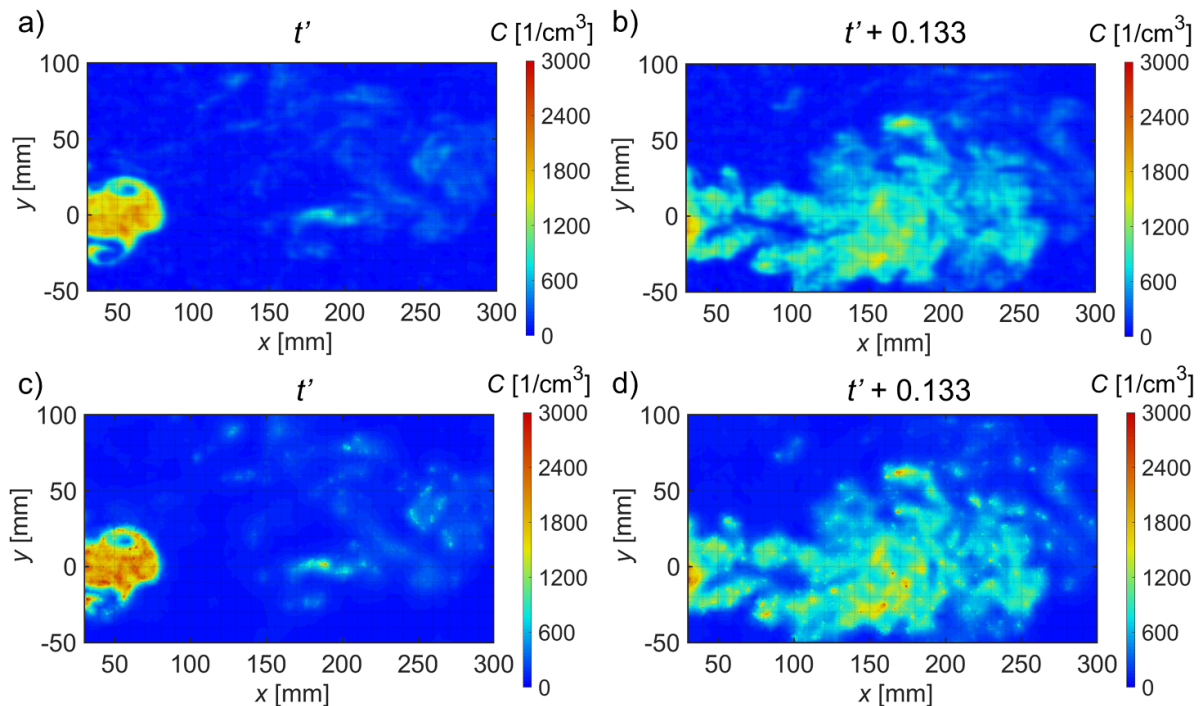


Figure 11. The concentration contour obtained by (a) and (b) the sliding average method with $l = 16$ pixel and intensity threshold of 800 counts; (c) and (d) Voronoi cell method with cut off criterion ($K_C = 30$) and minimum length scale $\lambda = 6$ mm. The results are for same instances as in velocity field in figure 10, i.e. instances t' (a) and (c) and $t' + 0.133$ (b) and (d).

4.3. Experimental results with a pulsatile jet

A pulsatile jet of air nebulized with DEHS particles (mean diameter $\approx 0.4 \mu\text{m}$) into a closed room is visualized as an example case with concentration variation. The air is heated through a water bath maintained at 37°C and led to the source of circular cross section of diameter 3 cm. The air is driven by displacement method which is controlled to provide a defined volume of air at a defined frequency. The measurement equipment and the setup is the same as that utilized for the uniform cases such that the concentration calibration could be utilized in determining the concentration distribution with the case presented here.

The PIV images are captured at specific phases of the cycle to facilitate phase averaging. A total of 30 instances are acquired within the cycle time period. For illustration, instances at time t' and $t' + 0.133$ (non-dimensionalized by the cycle time) are considered, where the latter instance is the

moment when the turbulent puff is still within the visualized window.

The obtained velocity field V (absolute velocity magnitude) for the case with a total volume of 1000 ml and 16 cycles/minute is shown in figure 10.

The resulting concentration profile for the instantaneous PIV images for two time instances is shown in figure 11. The concentration calibration shown in figure 8 is applied for the Voronoi method. For the sliding average method, similar calibration curve is obtained and utilized here to find the concentration contour. For a closer look, the comparison between the methods along the $y = 0$ line is plotted in figure 12. It can be observed from figures 11 and 12 that qualitatively both the methods reveal similar structures on the larger scales. However, the Voronoi method reveals finer details and sharper variation in the concentration contour, particularly at high concentration. At low concentrations, the Voronoi method does

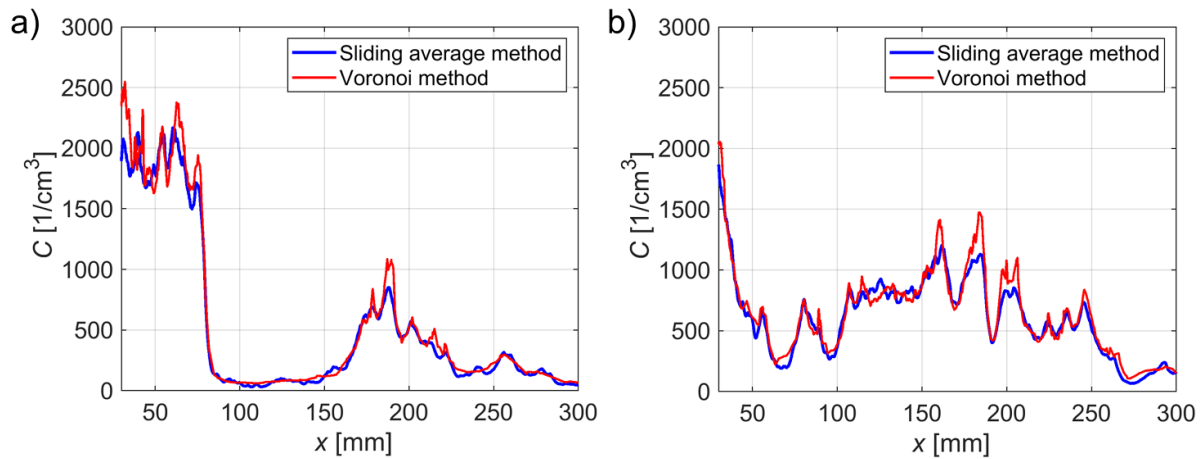


Figure 12. The concentration profile comparison with sliding average method and Voronoi method (as presented in figure 11) along the $y = 0$ line at time instances: (a) t' and (b) $t' + 0.133$.

not reveal the oscillations associated with the marker-shot noise.

5. Conclusion and summary

In this study, we focus on the determination of particle concentration using images acquired from PIV. We investigate and analyze two distinct methods for concentration determination: the sliding average method and the Voronoi cell-based method. Synthetic data of a diffusion problem, featuring an initial step in concentration, is utilized to explore the characteristics and limitations of each approach. In addition to the aforementioned methods, we introduce a modified Voronoi method with a criterion to select a certain number of cells to average. This method effectively captures large range of concentration regions and features including initial jump conditions in a diffusion problem. This new method offers flexibility by allowing adjustment of the minimum physical length scale and variation with respect to natural variations due to Brownian motion.

Furthermore, calibration of the visualized images with respect to particle counter revealed particle–particle overlap at higher concentration which is described by theoretical consideration. The described methods were applied to a real experimental case of turbulent puff. It is shown that the Voronoi method is able to capture small structures with high concentrations, while providing reliable results also in regions with low concentrations.

The advantages of the sliding average method are: (a) the relatively simple computations, and (b) the integral value of the concentration is the sum of the particle images. The benefits with Voronoi method are: (a) the adaptive length scale, (b) the control over feature length scale, while still maintaining minimum number of points for reliable local concentration. The computational effort for the Voronoi method could mean that it is more logical to apply when one is interested in understanding the features in instantaneous images. When one is interested in overall average field, sliding average method does give the necessary information when averaged over many snapshots.

Data availability statement

The data cannot be made publicly available upon publication because they are not available in a format that is sufficiently accessible or reusable by other researchers. The data that support the findings of this study are available upon reasonable request from the authors.

Acknowledgments

This research is funded by dtcc.bw—Digitalization and Technology Research Center of the Bundeswehr through project LUKAS which we gratefully acknowledge. dtcc.bw is funded by the European Union—NextGenerationEU.

ORCID iD

Abhilash Sankaran  <https://orcid.org/0000-0003-4105-2037>

References

- Balluffi R W, Allen S M and Carter W C 2005 *Kinetics of Materials* (Wiley)
- Billingsley P 1995 *Probability and Measure* (Wiley)
- Callister W D and Rethwisch D G 2018 *Materials Science and Engineering: An Introduction* (Wiley)
- Cierpka C, Lütke B and Kähler C J 2013 Higher order multi-frame particle tracking velocimetry *Exp. Fluids* **54** 1–12
- Daune M 1999 *Molecular Biophysics: Structures in Motion* (Oxford University Press)
- Gnirß M and Tropea C 2008 Simultaneous PIV and concentration measurements in a gas-turbine combustor model *Exp. Fluids* **45** 643–56
- Kähler C J, Hain R and Fuchs T 2023 Assessment of mobile air cleaners to reduce the concentration of infectious aerosol particles indoors *Atmosphere* **14** 698
- LaVision 2021 *Product Manual DaVis 10.2 Software* (LaVision GmbH)
- Li Y, Blois G, Kazemifar F and Christensen K T 2021 A particle-based image segmentation method for phase

- separation and interface detection in PIV images of immiscible multiphase flow *Meas. Sci. Technol.* **32** 095208
- Lukin A 2007 Tips & tricks: fast image filtering algorithms *JiS* **12** 2
- Maas H G 1992 Digitale Photogrammetrie in der dreidimensionalen Strömungsmesstechnik *PhD Thesis* ETH Zürich
- Monchaux R, Bourgoin M and Cartellier A 2010 Preferential concentration of heavy particles: a Voronoi analysis *Phys. Fluids* **22** 103304
- Newland E L and Woods A W 2023 On particle fountains in a crossflow *J. Fluid Mech.* **964** A10
- Nguyen C V, Carberry J and Fouras A 2012 Volumetric-correlation PIV to measure particle concentration and velocity of microflows *Exp. Fluids* **52** 663–77
- Nishino K, Kato H and Torii K 2000 Stereo imaging for simultaneous measurement of size and velocity of particles in dispersed two-phase flow *Meas. Sci. Technol.* **11** 633
- Okabe A, Boots B, Sugihara K and Chiu S N 2000 *Spatial Tessellations: Concepts and Applications of Voronoi Diagrams* (Wiley)
- Prasad A K 2000 Stereoscopic particle image velocimetry *Exp. Fluids* **29** 103–16
- Säid N M, Mhiri H, Le Palec G and Bournot P 2005 Experimental and numerical analysis of pollutant dispersion from a chimney *Atmos. Environ.* **39** 1727–38
- Sankaran A, Pawłowska S, Pierini F, Kowalewski T A and Yarin A L 2020 Dynamics of electrospun hydrogel filaments in oscillatory microchannel flows: a theoretical and experimental approach *Phys. Fluids* **32** 072008
- Schaap W E and Van De Weygaert R 2000 Continuous fields and discrete samples: reconstruction through Delaunay tessellations (arXiv:astro-ph/0011007v1)
- Shah Y, Kurelek J W, Peterson S D and Yarusevych S 2021 Experimental investigation of indoor aerosol dispersion and accumulation in the context of COVID-19: effects of masks and ventilation *Phys. Fluids* **33** 073315
- Tang M, Zhu N, Kinney K and Novoselac A 2020 Transport of indoor aerosols to hidden interior spaces *Aerosol Sci. Technol.* **54** 94–110
- Vincent J H 2007 *Aerosol Sampling: Science, Standards, Instrumentation and Applications* (Wiley)
- Warner S O and Smith B L 2014 Autocorrelation-based estimate of particle image density for diffraction limited particle images *Meas. Sci. Technol.* **25** 065201
- Weber L, Gabriel S and Class A G 2023 On the statistical evaluation of bubbly flows using Voronoi cells grouped in clusters with fixed cell count *Phys. Fluids* **35** 053311
- Zhang Y, Gu Z and Yu C W 2020 Impact factors on airflow and pollutant dispersion in urban street canyons and comprehensive simulations: a review *Curr. Poll. Rep.* **6** 425–39